

A unique determination of boundary condition in quantitative electron diffraction: Application to accurate measurements of mean inner potentials

L. Wu^a, M.A. Schofield^a, Y. Zhu^{a,*}, J. Taftø^b

^a *Department of Materials Science, Brookhaven National Laboratory, Building 480, Upton, NY 11973, USA*

^b *University of Oslo, P.O.Box 1048 Blindern, Oslo 0316, Norway*

Received 27 March 2003; received in revised form 10 June 2003

Dedicated to Professor Fang-hua Li on the occasion of her 70th birthday

Abstract

We combine off-axis electron holography and electron shadow imaging to accurately determine the specimen thickness and the incident electron beam direction over the illuminated area of a crystal. We, furthermore, quantify the variations in diffraction intensity with position over the same area. This unique solution to the experimental boundary condition problem enables us to make precise measurements of mean inner electrostatic potentials and structure factors that are sensitive to the bonding characteristics of materials. In this paper, we present the results of mean-inner potential determination from silicon and the newly discovered magnesiumdiboride superconductor.

© 2003 Elsevier B.V. All rights reserved.

PACS: 61.14.Lj; 61.14.Nm; 68.37.Lp; 74.70.Ad

Keywords: Convergent beam electron diffraction; Electron holography; Mean inner potential; Magnesium diboride

1. Introduction

Since electrons interact strongly with matter, transmission electron microscopy is limited to the study of thin regions of materials, usually of thickness much less than 1 μm . Furthermore, the amplitude and phase of the electron wave-field exiting a specimen changes drastically with sub-milliradian tilt of the incident beam direction, or

with nanometer variation in crystal thickness. Thus, for electron microscopy and diffraction to become quantitative on a general basis we need to know precisely the specimen thickness and incident beam direction as a function of position within the illuminated area of the specimen. Lack of ability to handle the boundary conditions on the small regions we are dealing with, has resulted in the view that electron diffraction a qualitative technique. We show in this paper that by combining off-axis electron holography (For example see Ref. [1]) and convergent beam electron diffraction with the electron beam cross-over several tens of

*Corresponding author. Tel.: +1-631-344-3057; fax: +1-631-344-4071.

E-mail address: zhu@bnl.gov (Y. Zhu).

micrometers above the specimen [2,3] we can accurately map the local thickness, i.e., uniquely determine the boundary conditions. In addition, we record in one single exposure the diffraction intensities over a wide range of angles and thicknesses from these convergent beam diffraction patterns, referred to as parallel recording of dark-field images (PARODI). We demonstrate the determination and uniqueness of the experimental boundary conditions using silicon as an example where the crystal structure parameters are better known than for any other materials. After having established the strength of the technique, we apply it to study the newly discovered MgB_2 superconductor where we determine the mean inner electrostatic potential and refine the structure factors of the innermost reflections. (The structure factors of MgB_2 will be published separately.) The mean inner potential and structure factors are very sensitive to bonding and closely tied to the superconducting properties since they are associated with the occupied electronic states near the Fermi level [4]. Measurement of these physical parameters may shed light on the high superconducting transition temperature of 39 K in this structurally simple compound.

2. Experimental considerations

The principles of off-axis holography and PARODI are shown in Fig. 1. For more details see for example Refs. [1–3]. The holography and PARODI experiments were carried out using 300 keV electrons in a JEOL 3000F field-emission TEM equipped with electrostatic biprism and Gatan imaging filter (GIF). The retractable biprism assembly used for the electron holography experiments consists of a platinum wire $<0.6\ \mu\text{m}$ in diameter located approximately in the selected area aperture plane of the microscope, and is rotatable $\pm 90^\circ$. In PARODI experiments, we focus the electron probe above the sample, as illustrated in Fig. 1(a). In doing so, we form shadow-images (mainly dark-field images) of a large illuminated area within the diffraction-disks that contain not only orientation information (as with conventional convergent beam

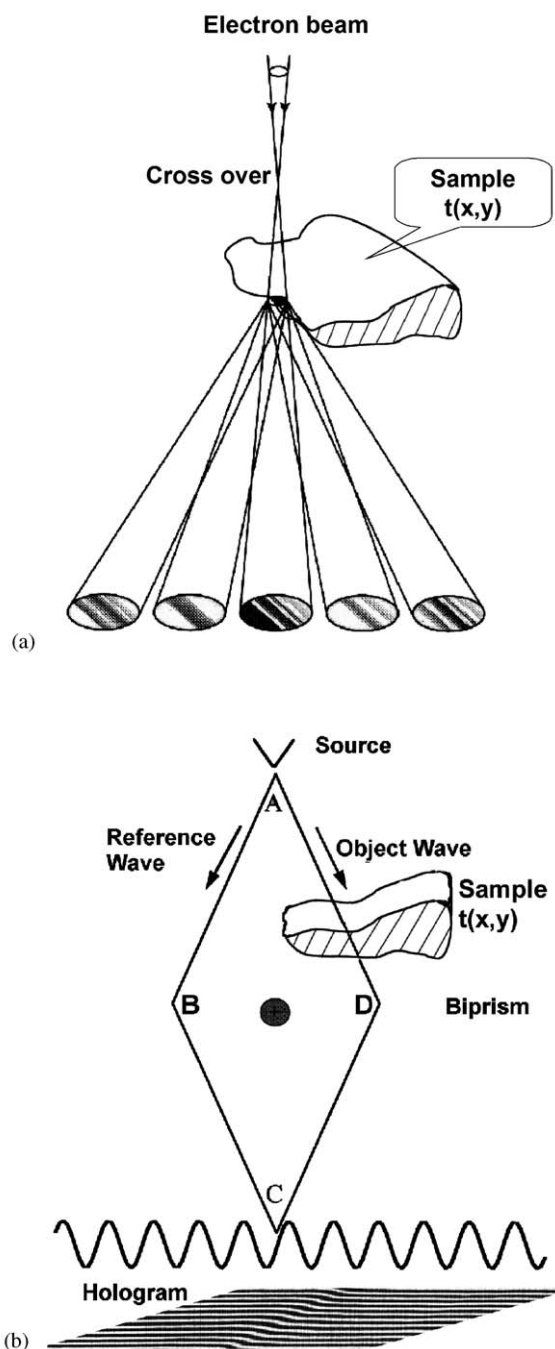


Fig. 1. Schematics of the experimental set up for: (a) PARODI; and (b) off-axis electron holography.

electron diffraction), but also thickness profiles, or Pendellösung plots, for the many simultaneously recorded reflections. The thickness profile usually increases from zero to a maximum value that can range from ten to several hundred nanometers depending on the distance from the specimen to the beam crossover. Previously, our PARODI experiments were focused on wedge specimens, i.e., samples with linear thickness increase from the specimen edge for quantitative electron diffraction analysis where we have measured variation of diffraction intensity as a function of thickness. In practice, however, such an ideal wedge is not always available. Here, we use off-axis electron holography to obtain thickness maps of the illuminated area having an arbitrary thickness distribution. A well-characterized multi-scan CCD camera [5] located after the GIF was used to record both holograms and PARODI patterns.

We studied fragments of Si obtained by crushing a piece of bulk Si. The fragments of Si on our holy carbon film have irregular wedges with a wide range of wedge angles. We avoid wedges that are too shallow or too steep. Shallow wedges tend to bend. Steep wedges are demanding with respect to spatial resolution, and may cause an additional need for correction due to the change in the direction of the transmitted electrons by refraction. We recorded energy filtered PARODI patterns and, subsequently, holograms from the same area. The holography experiments were carried out after having tilted the specimen on the order of 1° to avoid strong Bragg reflections and, therefore, minimizing the dynamical effects in the hologram. Fig. 2 shows an experimental hologram and the phase contour map reconstructed from a hologram obtained by applying a 13 V bias to the wire of the biprism. The equiphase contours are separated by $\Phi = \pi$ rad. The phase, Φ , can be converted to thickness t by the formula:

$$\Phi = CV_0 t. \quad (1)$$

If the mean inner potential, V_0 , of Si was accurately known, since at 300 keV the constant

$$C = \frac{2\pi}{\lambda E} \frac{E + E_0}{E + 2E_0} = 0.00652 \text{ rad/V nm}. \quad (2)$$

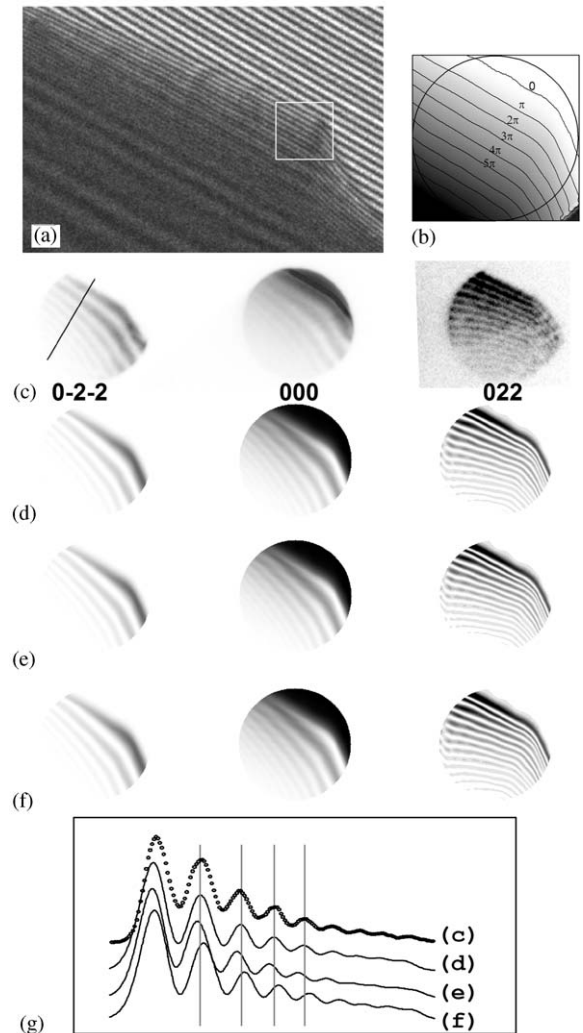


Fig. 2. Experimental observations and calculations for Si: (a) experimental hologram; (b) reconstructed phase map of the boxed area in (a) with equiphase contour intervals being π . (c–f) PARODI patterns of the same area (circled in (b)) showing the 011 diffraction row. The $[1\bar{1}-1]$ zone with the center of Laue circle at $-14.2, 6.55, -7.65$ position; (c) energy filtered experimental pattern; (d–f) calculated patterns based on the phase map obtained from the hologram (a), using a scaling factor of $1/CV_0 = 13.33 (V_0 = 11.5), 13.94 (V_0 = 11.0),$ and $12.78 (V_0 = 12.0) \text{ nm/rad}$, respectively. The contrast of the 022 disk was enhanced for better visibility; (g) the intensity profiles of the line-scans in the 0–2–2 disks at the position marked in (c). The comparison of the intensity maxima suggests the best fit is (d) with the mean potential of 11.5 V.

Here, λ is the wavelength of the incident electrons, E their kinetic energy, and E_0 the rest mass of an electron. Conversely, the mean inner potential can be determined from Eq. (1) if the sample thickness was accurately known. Indeed, the experimentally determined mean inner potential of Si ranges between 9.3 and 12.1 V [6–8], where the major reason for this discrepancy is the difficulty in accurately determining the thickness of the sample.

Most experiments aimed at determining the mean inner potential are based on a priori knowledge of the geometry of the sample by considering surface energies and cleavage planes, or considering particles with well-defined geometrical shapes. Usually the wedges between these facets are steep implying densely spaced fringes in the hologram, and thus the need for high spatial resolution. Such close fringes are easily washed out with thickness so that it becomes difficult to measure the phase shift in thicker regions where the accuracy increases. Furthermore, the incident beam directions, where there is a simple relationship between the distance from the sample edge and the specimen thickness t , tend to be zone axes where many reflections, or Bloch waves, are excited. These Bloch waves see potentials that are different from the mean inner potential. To circumvent these difficulties, our approach is to use the reconstructed phase maps from the holography experiments as thickness maps (up to an unknown scaling factor equal to the mean inner potential), and to combine this information with results from the PARODI experiments performed on the same sample region. The mean inner potential then becomes a free parameter in fitting the PARODI patterns, which we discuss next.

3. Calculations of shadow images of the PARODI pattern

The wave function of a diffracted beam at the exit surface of the specimen can be calculated using the Bloch wave method [9,10] for fast electrons:

$$\phi_g = \sum_{j=1}^N c_j C_g^j \exp(2\pi i \gamma^j t), \quad (3)$$

$$I_g = \phi_g \cdot \phi_g^*. \quad (4)$$

Here the eigenvector coefficients C_g and eigenvalue γ are given by

$$A \begin{pmatrix} C_0 \\ C_g \\ C_h \\ \vdots \end{pmatrix} = \begin{pmatrix} 0 & U_{-g} & U_{-h} & \cdots \\ U_g & 2KS_g & U_{gh} & \cdots \\ U_h & U_{hg} & 2KS_h & \cdots \\ \vdots & \vdots & \vdots & \ddots \end{pmatrix} \begin{pmatrix} C_0 \\ C_g \\ C_h \\ \vdots \end{pmatrix} = 2K_n \gamma \begin{pmatrix} C_0 \\ C_g \\ C_h \\ \vdots \end{pmatrix}, \quad (5)$$

where U_g is the electron structure factor in units of \AA^{-2} and the excitation error, $2KS_g = K^2 - (K + g)^2$, with K the incident beam wavevector. If including absorption, the matrix A is, in general, complex. Eq. (5) is a standard equation that can be diagonalized by using LAPACK computer codes [11], and the excitation coefficients c_j are obtained by applying boundary conditions at the entrance surface of the specimen.

For diffraction patterns with a parallel illumination, i.e., with only one incident beam direction, we need only solve Eq. (5) once. For conventional convergent-beam electron diffraction (cCBED), we focus the incident beam on the sample and a disk pattern is formed at the back focal plane of the objective lens where the disk size depends on the convergent angle of the illumination. Each point in the central disk is assumed to originate from the same point of the specimen, but with a different incident beam direction given by:

$$K_r = K_0 + r^*, \quad (6)$$

where K_0 is the beam direction at the center of the disk taken to be the coordinate origin and r^* the position vector of the point. Eq. (5) is solved to obtain the eigenvector and eigenvalue for each point, and the diffraction intensity for each point is then calculated by Eqs. (3) and (4). For cCBED, since the illuminated area is very small, the thickness is considered to be a constant. The intensity oscillation within the disks is caused by the variation of the incident beam direction or excitation error.

In PARODI experiments, where we focus the beam above the sample (Fig. 1a), an extended region of the sample is illuminated. The size of the illuminated area depends on the distance from the specimen to the cross-over and convergence angle. Similar to cCBED, a disk pattern is formed in the back focal plane. Each point in the disk corresponds to an incident beam direction which can be obtained by the Eq. (6) as with cCBED. Unlike cCBED, however, each point in the disks comes from different points of the sample, which, generally, have different thicknesses. Thus, a shadow image of the illuminated area is formed in the disk, or, equivalently, a bright-field image is formed in the transmitted disk, and dark-field images in diffracted disks. Therefore, the intensity oscillation inside the disks depends not only on incident beam direction but also on the sample thickness. The calculation of PARODI patterns is essentially the same as that of cCBED but replacing the constant thickness with a thickness map $t(x, y)$ in Eq. (3). The thickness map can be calculated for the illuminated area if there exists a well-defined geometry, e.g. wedge with linear relationship between the position and thickness, as we have previously used for the PARODI experiments. In the present study we use off-axis electron holography to experimentally map the nonlinear thickness distribution over the area of interest. The thickness map was then used as a 2-D template for diffraction calculations.

4. Applications

4.1. Mean inner potential of Si

In our experiments, PARODI patterns and holograms are collected from the same area where we suppose $t(x, y)$ is the thickness of the specimen and $k(x, y)$ the crystallographic direction of the incident beam. Here, (x, y) are the 2D coordinates in the specimen plane. Provided the specimen is not bent over the illuminated area, we know $k(x, y)$ from the PARODI pattern and $t(x, y)$ from the hologram. Thus, we know the experimental boundary conditions. Since the structure parameters including structure factors and thermal

parameters are well known for Si, we can calculate the PARODI patterns without any fitting parameters other than the mean inner potential, as discussed above. That is to say, the absolute thickness scale relies on knowing the mean inner potential of Si. If we start by assuming a mean inner potential of say 10 V we need to adjust this value until the experimental and calculated PARODI patterns fit. We arrive, consequently, at an experimentally derived value for the mean inner potential.

Figs. 2(c)–(f) show the PARODI patterns of the 011 systematic diffraction row in Si with the center of the Laue circle at $-14.2, 6.55, -7.65$ position. The orientation was reached by tilting the crystal 3.6° around the $[011]^*$ axis from the $[11-1]$ zone and corresponds to $[0-2-2]$ near the Bragg position. The energy filtered experimental pattern is shown in Fig. 2(c). The calculated patterns shown in Figs. 2(d)–(f) are based on the phase map obtained from the hologram in Fig. 2(b) using scaling factors of $1/CV_0 = 13.33, 13.94$ and 12.78 nm/rad , respectively, to convert the phase to thickness. The contrast of the 022 disk was enhanced for better visibility. The intensity oscillations of line-scans in the $0-2-2$ disks from the position marked in Fig. 2(c) is plotted in Fig. 2(g). Comparison of the intensity maxima suggests Fig. 2(d) is the best fit with a scaled thickness that corresponds to an inner potential of 11.5 V, while relatively poor agreement with experiment for Fig. 2(e) ($V_0 = 11.0 \text{ V}$) and Fig. 2(f) ($V_0 = 12.0 \text{ V}$). The calculations include over 100 beams. The thickness variation in the entire illuminated area, or the PARODI disks, arranges from 0 (vacuum) to 480 nm.

4.2. Mean inner potential of MgB_2

Similar experiments were done on the newly discovered superconductor MgB_2 . Fig. 3(a) shows an experimental hologram and the reconstructed phase map, Fig. 3(b), with superimposed π -interval contours. Fig. 3(c) is an energy filtered experimental PARODI pattern of the same area showing the 101 diffraction row with the 101 reflection near the Bragg position (center of the Laue circle is at $7.52, 5.71, 9.61$, which was tilted

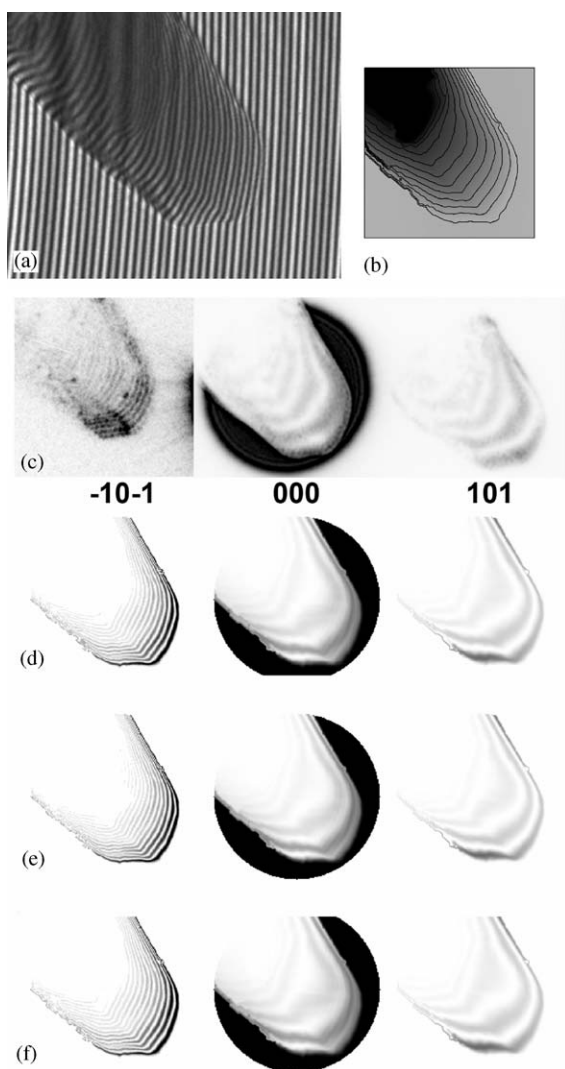


Fig. 3. Experimental observations and calculations for MgB_2 in the 101 diffraction row: (a) experimental hologram; (b) reconstructed phase map with equiphase contour intervals of π ; (c–f) PARODI patterns of the same area. The $[1\ 3\ -1]$ zone with the center of Laue circle at $-7.52, 5.71, 9.61$; (c) energy filtered experimental pattern. (d–f) Calculated patterns based on the thickness map obtained from the hologram (a) using the scaling factor of $1/CV_0 = 13.22(V_0 = 11.6), 14.33(V_0 = 10.7)$ and $12.27(V_0 = 12.5)$ nm/rad, respectively. The contrast of $-10-1$ disk was enhanced for clarity. The pattern in (d) gives the best fit to the experiment. The mean potential was determined to be $V_0 = 11.6$ V.

4.2° from the $[1\ 3\ -1]$ zone axis). Figs. 3(d)–(f) show the calculated patterns based on the thickness map obtained from the hologram (Figs. 3(a)

and (b)) assuming scaling factors $1/CV_0 = 13.22$ ($V_0 = 11.6$), $14.33(V_0 = 10.7)$ and $12.27(V_0 = 12.5)$ nm/rad, respectively. For clarity the contrast of the $-10-1$ disk is enhanced. The pattern in Fig. 3(d) gives the best fit to the experiment. The mean potential is determined to be $V_0 = 11.6$ V.

Another example of experiments and calculations for MgB_2 is shown in Fig. 4. Figs. 4(a) and (b) are the experimental hologram and reconstructed phase map with π -interval contours. Fig. 4(c) is the experimental PARODI pattern for the 001 diffraction row with the center of the Laue circle at $2.5, 5, 1.18$ (2.8° deviates from the $[2\ -1\ 0]$ zone). Figs. 4(d)–(f) are calculated PARODI patterns with experimentally refined structure factors and using $V_0 = 11.7$ (best fit), $V_0 = 10.8$ and 12.6 V, respectively. The value $V_0 = 11.7$ V obtained in this experiment agrees very well with the value $V_0 = 11.6$ V obtained in the experiment shown in Fig. 3 for MgB_2 . We note the error in the refinement of the scaling factor, or the mean inner potential, depends on several factors including quality of the sample, the signal/noise ratio of the holograms and PARODI patterns, and dynamic effects contributing to the phase maps reconstructed from the holograms (see Section 5). We illustrate here, however, the sensitivity of this technique to charge transfer and bonding within the crystal. The calculation based on the use of the scattering amplitudes of free atoms [12] and a mean inner potential of 11.7 V is shown in Fig. 4(g). (As opposed to $V_0 = 11.7$ V, but using refined structure factors in Fig. 4(d) representing the best experimental fit.) Fig. 4(h) plots the intensity profiles of line scans of the 002 disk at the position marked in Fig. 4(c). Comparison of the intensity maxima positions between calculations with experiment clearly illustrates that Figs. 4(e)–(g) do not give good fits to the experimentally observed PARODI pattern. It also illustrates that the technique is very sensitive to the charge transfer and bonding characteristics of the crystal. As seen in the calculated pattern (Fig. 4(g)), using scattering amplitudes of free-atoms, not only do the intensity maxima of the 002 disk disagree with the experiment, but also the intensity of the 001 disk is much too high.

5. Dynamic effects on the error analysis

In our quantitative analysis, we note the importance of error assessment in measuring the mean inner potential, especially to take the

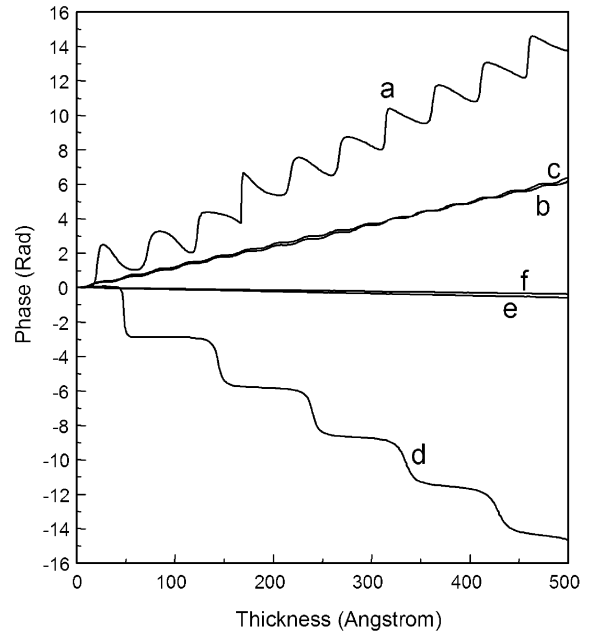
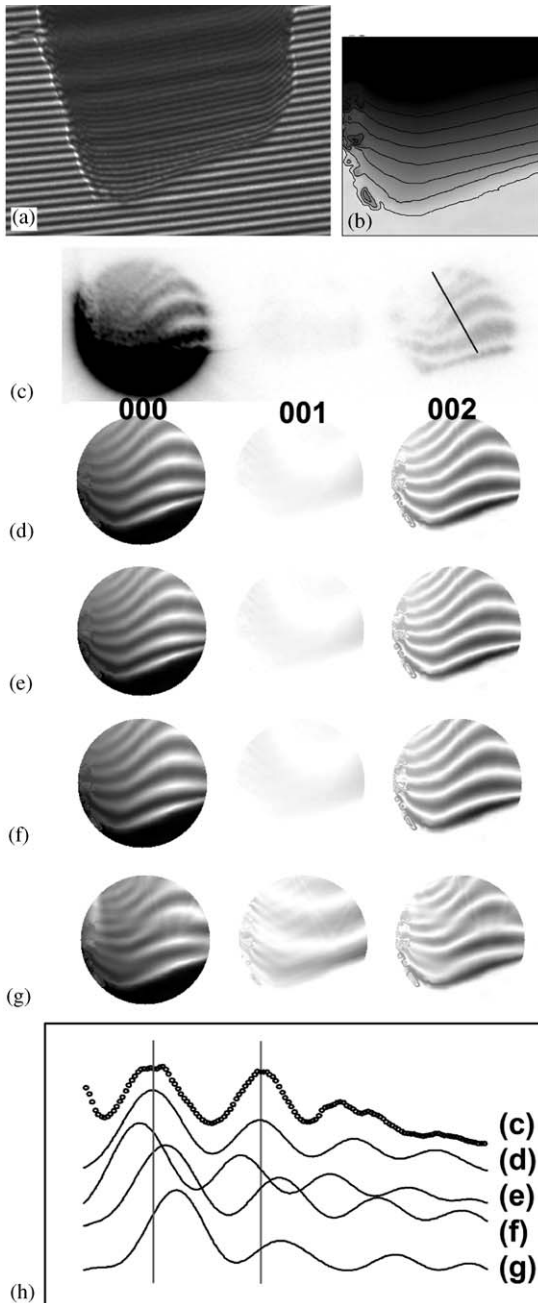


Fig. 5. Dynamical effects induced phase change, described by the term D as a function of thickness with different crystal orientations for MgB_2 . (a) $[100]$ zone; (b–f) $[2-10]$ zone with the center of Laue circle at: 0,0,0 (b); 2.5, 5, 0 (c); 2.5, 5, 1 (d); 2.5, 5, 3.5 (e); and 2.5, 5, 4.5 (f).

dynamic diffraction effects into account. Based on Bloch wave calculations described in Section 3, we are able to evaluate the changes in the phase shift (as measured with holography) introduced by the dynamic diffraction effects. Fig. 5 shows the phase change introduced by dynamical diffraction described by the term D (the phase term, we refer as D , of the wave function ϕ_{000} in Eq. (3)), as a function of thickness for MgB_2 with different

Fig. 4. Experimental observations and calculations for MgB_2 in the $00l$ diffraction row. (a) Experimental hologram; (b) reconstructed phase map with equiphase contour intervals of π . (c–g) PARODI patterns of the $[2-10]$ zone with the center of the Laue circle at 2.5, 5, 1.18. (d–g) Calculations with experimental refined structural factors: (d) best fit with $V_0 = 11.7$; (e) $V_0 = 10.8$; and (f) $V_0 = 12.6$ V; (g) calculation using neutral-atoms with $V_0 = 11.7$ V does not give good fit since the intensity of 001 disk is too high. (h) The intensity profiles of the line-scans in the 002 disks at the position marked in (c). The comparison of the intensity maxima suggests (c–g) do not agree with the experiment.

crystal orientations. We note that the dynamical effect is very strong when the crystal is at a low index zone as shown in (a) and (b) of Fig. 5. It is still quite strong when the crystal is tilted away from the zone axis to a systematic row orientation. The curve (c) in Fig. 5 is for the crystal tilted 2.8° around the $[001]^*$ axis from the $[2-10]$ zone, where the center of the Laue circle changes from 000 to 2.5, 5, 0 and only the 00/ reflections are strongly excited. The dynamical effect is even stronger when a reflection with a large structure factor is at the Bragg position as in Fig. 5(d). This is due to the strong dynamical coupling between the incident beam and diffracted beam. The phase oscillations are similar to the intensity oscillations as shown in Figs. 3 and 4. This strong dynamical coupling is, in fact, used to refine the scaling factor in PARODI patterns (see Figs. 3 and 4 and related text). However, the total phase retrieved from holography in this case will significantly deviate from that based on kinematical calculations using Eq. (1) since the phase shift due to the dynamical effect can amount up to 30% of the total phase change. Moreover, the nonlinear relationship between the dynamic effect term D and thickness t causes a divergence during refinement of the scaling factor in PARODI due to the nonlinear relationship between the phase map and the actual thickness distribution. Therefore, in the holography experiment, it is necessary to minimize the dynamical effect.

An obvious choice is to tilt the crystal, i.e., in this case, around the axis perpendicular to the $[001]^*$ direction to avoid exciting any strong reflections. An example for the center of Laue circle at 2.5, 5, 3.5 is plotted in Fig. 5(e), showing a linear relationship between D and thickness t with $D = \zeta t$ (ζ is a constant). The slope ζ is -0.0012 rad/nm, while the CV_0 is 0.075 rad/nm. The ratio of D to the total phase shift is reduced to 1.6%, and we are thus able to correct the dynamic effect, as reported by Gajdardziska-Josifovska et al. [6]. Further tilt of the crystal results in no strongly excited reflections and reduces D to less than 1% (Fig. 5(f), Laue circle: 2.5, 5, 4.5), where the error caused by dynamical effects is negligible. The tilt angle between (d) and (f) shown in Fig. 5 is only 1.1° .

While we may tilt the sample for holography experiments in order to reduce the dynamic effects, this introduces a change in the projected thickness of the sample relative to the PARODI experiments carried out on the same area. The thickness change associated with the tilt angle θ discussed above is $\Delta t/t = [\sin(\phi + \theta) - \sin(\phi)]/\sin(\phi)$, where ϕ is the angle made between the incident beam and sample surface. Except for sample wedges with steep facets, ϕ is generally larger than 60° , so the thickness change introduced by the 1.1° tilt is less than about 1%. In practice, we record the PARODI patterns under systematic row diffraction conditions and then tilt the crystal about 1° to record the holograms. The error introduced by such a procedure, including dynamic effects, can be limited to less than 2%.

6. Conclusions

In summary, combining the experimental techniques of PARODI and off-axis electron holography, we are now able to find a unique solution to the experimental boundary condition problem that is crucial to quantitative electron microscopy analysis. Using this new approach we can measure the mean inner potentials of crystals with a high accuracy that does not involve uncertainty with a priori knowledge of the thickness variation of the specimen. We thus determined the mean inner electrostatic potential to be 11.5 ± 0.5 V for Si and 11.7 ± 0.9 V for MgB_2 . Furthermore, the method can be used to accurately determine the structure factors of the innermost reflections of materials in order to address issues of charge transfer and valence electron distribution that are responsible for their functionality.

Acknowledgements

This work was supported by Division of Materials Sciences, Office of Basic Energy Science, US Department of Energy, under contract No. DE-AC02-98CH10886.

References

- [1] E. Volkl, L.F. Allard, D.C. Joy (Eds.), *Introduction to Electron Holography*, Plenum Press, New York, 1999.
- [2] J. Taftø, Y. Zhu, L.J. Wu, *Acta Cryst. A* A54 (1998) 532.
- [3] L.J. Wu, Y. Zhu, J. Taftø, *Phys. Rev. Lett.* 85 (2000) 5126.
- [4] Y. Zhu, A.R. Moodenbaugh, G. Schneider, T. Vogt, Q. Li, G. Gu, D.A. Fischer, J. Taftø, *Phys. Rev. Lett.* 88 (2002) 247002.
- [5] M.A. Schofield, Y. Zhu, L. Wu, V.V. Volkov, M. Malac, *JEOL News: Electron. Opt. Instrum.* 36E (2001) 2.
- [6] M. Gajdardziska-Josifovska, M.R. McCartney, W.J. de Ruijter, D.J. Smith, J.K. Weiss, J.M. Zuo, *Ultramicroscopy* 50 (1993) 285.
- [7] K.H. Gaukler, R. Schwarzer, *Optik* 33 (1971) 215.
- [8] Y.C. Wang, T.M. Chou, M. Libera, T.F. Kelly, *Appl. Phys. Lett.* 70 (1997) 1296.
- [9] A. Howie, High voltage electron microscopy: the theory of high-energy electron diffraction, in: S. Amelinckx, R. Gevers, J. Van Landuyt (Eds.), *Diffraction and Imaging Techniques in Materials Sciences*, North-Holland, Amsterdam, 1978, p. 457.
- [10] J.M. Zuo, *Mater. Trans. JIM* 39 (1998) 938.
- [11] E. Anderson, Z. Bai, C. Bischof, J. Demmel, J. Dongarra, J. Du Croz, A. Greenbaum, S. Hammarling, A. McKenney, S. Ostrouchov, D. Sorensen, *LAPACK Users' Guide*, The Society for Industrial and Applied Mathematics, 1999.
- [12] L. Wu, Y. Zhu, T. Vogt, H. Su, J.W. Davenport, J. Taftø, *Phys. Rev. B*, submitted for publication.